Fluoride-induced dynamic surface self-reconstruction produces unexpectedly efficient oxygen evolution catalyst

Bowei Zhang,[1] Kun Jiang,[2] Haotian Wang,[2] & Shan Hu[*1]

1. Department of Mechanical Engineering, Iowa State University, Ames, Iowa 50011, United States

2. Rowland Institute, Harvard University, Cambridge, Massachusetts 02142, United States

KEYWORDS: Nickel-iron hydroxide, surface reconstruction, OER, electrocatalysis, nanostructure

ABSTRACT

Oxygen evolution reaction (OER) is a key process in water splitting systems, fuel cells, and metal-air batteries, but the development of highly active and robust OER catalyst by simple methods is a great challenge. Here, we report an *in situ* dynamic surface self-reconstruction that can dramatically improve the catalytic activity of electrocatalysts. The fluoride (F^-)-incorporated NiFe hydroxide (NiFe-OH-F) nanosheets array was initially grown on Ni foam by a one-step hydrothermal method, which requires a 243 mV overpotential (η) to achieve 10 mA cm^{-2} current density (j) with a Tafel slope of 42.9 mV dec^{-1} in alkaline madia. After the surface self-reconstruction induced by fluoride leaching under OER conditions, the surface original NiFe-OH-F was converted into highly mesoporous and amorphous NiFe oxide hierarchical structure and the OER activity increases over 58 folds at η = 220 mV. The corresponding η at 10 mA cm^{-2} decreases to 176 mV with an extreme low Tafel slope of 22.6 mV dec^{-1}, this performance is superior to the state-of-the-art OER electrocatalysts.

High-performance electrocatalysts play vital roles in many energy conversion and storage systems. Currently used catalysts for oxygen evolution reaction (OER) — an reaction central to water splitting technologies,[1,2] fuel cells,[3] and metal-air batteries[3,4] — are typically the high-cost and scarce noble-metal oxides (RuO_2/IrO_2). Moreover, large overpotentials (η) to drive the reaction decrease the energy conversion efficiency and impede the practical application of devices. Enormous efforts have therefore been devoted to developing alternative OER catalysts based on the first-row transition metals.[5,6]

Among the numerous reported non-noble compounds, $NiFeO_xH_y$ exhibits extraordinary inherent catalytic activity for OER and has been regarded as the most active non-noble OER catalyst in alkaline conditions, but the η is still large and cannot satisfy the practical applications.[7–10] To improve the activity, Xu *et al.* reported exfoliating NiFe layered double hydroxide into single layer nanosheets.[11] The exfoliated Ni-Fe hydroxide nanosheets were further integrated with defective graphene by Jia *et al.*, which delivers a 10 mA cm^{-2} at η = 210 mV in 1M KOH.[12] In 2017, NiFe hydroxide nanosheets were grown on copper nanowires by a multiple-step method and broken the milestone overpotential of 200 mV in 1M KOH ($\eta_{10\ mA\ cm^{-2}}$ = 199 mV).[13] To further improve the OER performances of $NiFeO_xH_y$, anions (-Se, -S, -N, -B and -P) and defects (cation/anion vacancies) have been introduced into it and a series of progresses have been achieved in recent few years.[5,6,22,23,14–21] Despite the reported high efficiency, the synthesis routes of the above methods are complex, hazardous, and environmentally-unfriendly with low yields.[20,24,25] This prompted us to explore safer and more scalable methods to synthesize efficient NiFe-based OER electrocatalysts.

Hydrothermal growth is a facile method for the fabrication of NiFe hydroxide and ammonia fluorine (NH_4F) is frequently used as a precursor.[18,22,26–29] Existing studies ascribe the main

function of the NH_4F to the anion fluoride (F^-) for its ability to enhance the mechanical adhesion between the hydroxide and the substrate.[26,27] A recent study by our group has discovered that F^- has been introduced into the hydrothermally grown NiFe hydroxide and has significantly influenced its catalytic activity for the hydrogen evolution reaction (HER).[30] It is to our surprise that few efforts have been devoted to investigating the effects of F^- on the OER catalysts so far, although this investigation is much needed considering that the introduction of other anions (-Se, -S, -N, -B and -P) have shown to greatly enhance the OER activity of $NiFeO_xH_y$.

Herein, we fabricated the fluoride incorporated NiFe hydroxide nanosheets on three-dimensional (3D) nickel foam (NiFe-OH-F) by a one-step hydrothermal method and reported a phenomenon that the fluoride in NiFe hydroxide can leach out under OER conditions and then induce chemical evolution and *in situ* surface self-reconstruction. After the electrochemical tuning under OER conditions, significant amount of the fluoride was removed from NiFe-OH-F and the original surface layer was transformed into mesoporous and amorphous NiFe oxide layer. The OER activity of the surface reconstructed NiFe-OH-F (denoted as NiFe-OH-F-SR) electrode was improved by ~ 58 folds compared to the original NiFe-OH-F nanosheet arrays. This work provides a simple and scalable strategy for the synthesis of highly active nano-electrocatalysts, by *in situ* surface self-reconstruction, which are difficult to gain access to by conventional synthesis routes.

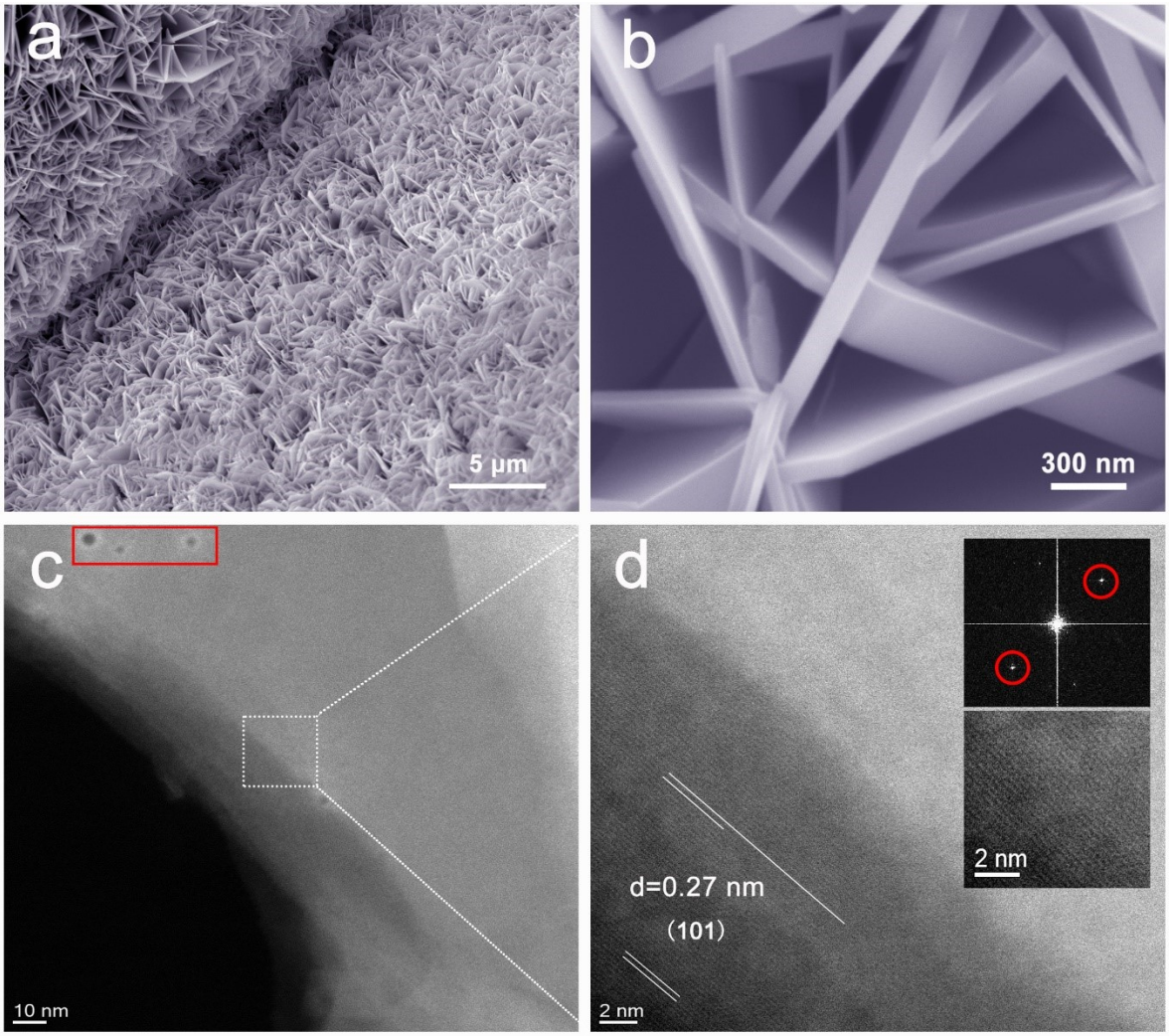

Figure 1. Characterization for NiFe-OH-F nanosheets. (a) SEM image of NiFe-OH-F nanosheets grown on nickel foam. (b) Magnified SEM image and (c) high resolution HAADF-STEM image. (d) Lattice spacing and the corresponding FFT images.

We initially synthesized the fluoride-incorporated nickel iron hydroxide (NiFe-OH-F) nanosheet arrays on 3D Ni foam by a hydrothermal method to characterize its structure and morphology. The microscopic structure of Ni foam is shown in the Figure S2. The photograph in Figure S3 indicates that the NiFe-OH-F layer was uniformly coated on Ni foam. SEM images in Figure 1a and b show the layer is composed of an array of vertically grown nanosheets with smooth surface. The smooth surface of NiFe-OH-F nanosheets was further confirmed by the high resolution high-angle-annular-dark-field scanning transmission electron microscopy (HAADF-STEM) image in Figure 1c. Note that the few pores in the red rectangle in Figure 1c are caused by the high-voltage electron beam during STEM characterization. The lattice spacing of 0.27 nm and Fast Fourier transformation (FFT) image in Figure 1d index to the (101) facet of NiFe hydroxide.[30]

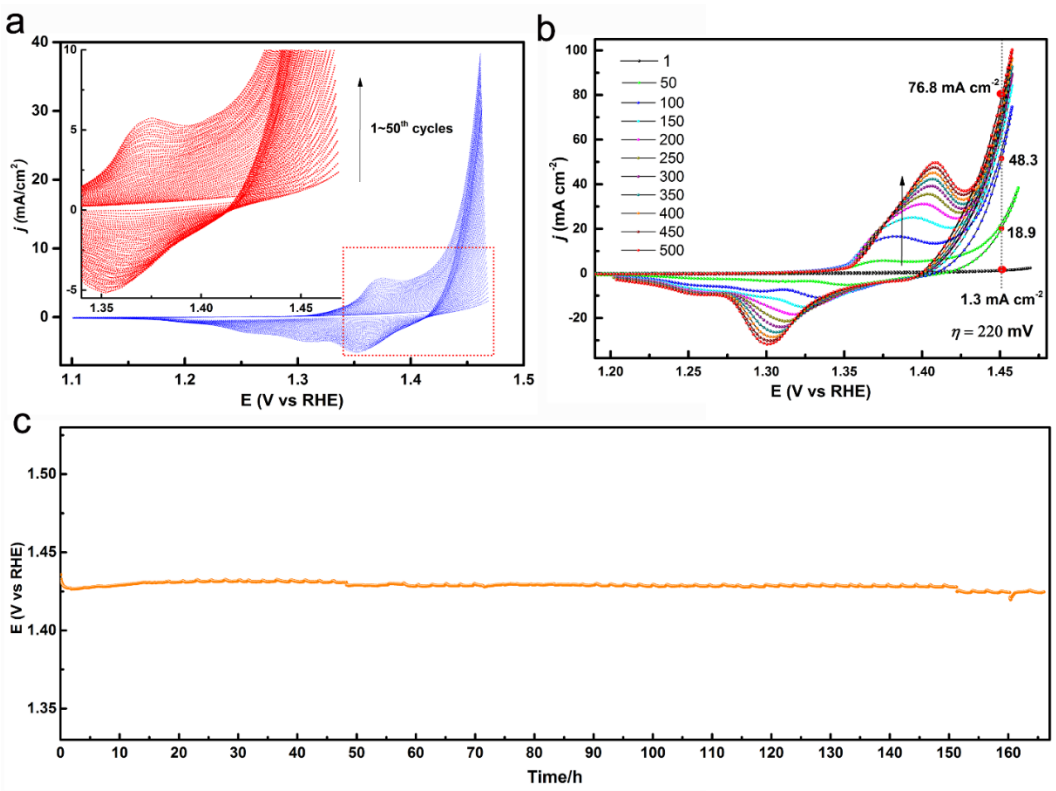

Figure 2. Electrochemical tuning and OER durability. (a) The first 50 CV cycles and (b) the entire 500 CV cycles for NiFe-OH-F. (c) Durability test of the post-cycling NiFe-OH-F electrode at j = 50 mA cm^{-2} for over 165 h in a new electrolyte (1M KOH).

To preliminarily investigate the OER performance and stability of NiFe-OH-F, a typical cyclic voltammetry (CV) cycling was carried out in 1M KOH medium at a scan rate of 5 mV s^{-1} without *iR*-compensation. Unexpectedly, the OER current and the areas of Ni oxidation ($Ni(OH)_2$/NiOOH) peak increase gradually following the cycling in the first 50 cycles (Figure 2a). To exclude the interference of Ni foam substrate, we then cycled the bare Ni foam for 50 cycles under the same conditions and did not found significant OER current in this potential range (Figure S4). As NiFe-OH is a well-known stable OER electrocatalyst under alkaline condition,[9,13,31–33] the phenomenon

here on NiFe-OH-F is interesting and needs to be further investigated. Thus, the electrode was furtherly cycled at the same conditions until the OER current became stable. As shown in Figure 2b, the OER current increases rapidly before the 150th cycle and stabilizes after 400 cycles. Compared to the current density at the 1st cycle, the OER current densities at the 50th cycle (18.9 mA cm^{-2}), 100th cycle (48.3 mA cm^{-2}), and 500th cycle (76.8 mA cm^{-2}) were increased by about 14, 36, and 58 folds, respectively, at η = 220 mV. More interestingly, dramatic increases in the Ni oxidation peak area can be observed from Figure 2b as well as the significant negative shifts in the onset potential. The oxidation peak area can be integrated and assigned to the total charge transfer to determine the extent of the $Ni(OH)_2$/NiOOH transformation. This result indicates that the $Ni(OH)_2$/NiOOH transformation was dramatically increased for the post-cycling NiFe-OH-F. The resultant NiOOH phase after $Ni(OH)_2$/NiOOH oxidation is believed to be crucial to the active sites of NiFe hydroxide for OER (Figure 2a and b).[34–36] In Figure 2b, the oxidation peak of $Ni(OH)_2$/NiOOH shifts significantly towards higher potential in the CV cycling, indicating that the CV cycling alters the oxidation properties of Ni (i.e. the average valence of Ni) and then lead to a concurrent increase of catalysis activity of Ni cations toward the OER.[36]

The stability of the post-cycling NiFe-OH-F was tested and shown in Figure 2c. In 1M KOH, the potential required to deliver a current density of 50 mA cm^{-2} is ~ 1.43 V vs RHE, and stabilizes around this value for over 165 h, with very small potential fluctuations (< 10 mV). After the long-term stability test, ICP-MS was used to measure the corresponding electrolyte as well. As shown in Table S1, no Fe element was detected in the electrolyte and the amount of Ni element is negligible. The stabilized OER performance and the excellent stability demonstrated by the post-cycling NiFe-OH-F outperformed most recently reported OER electrocatalysts (see Table S2).

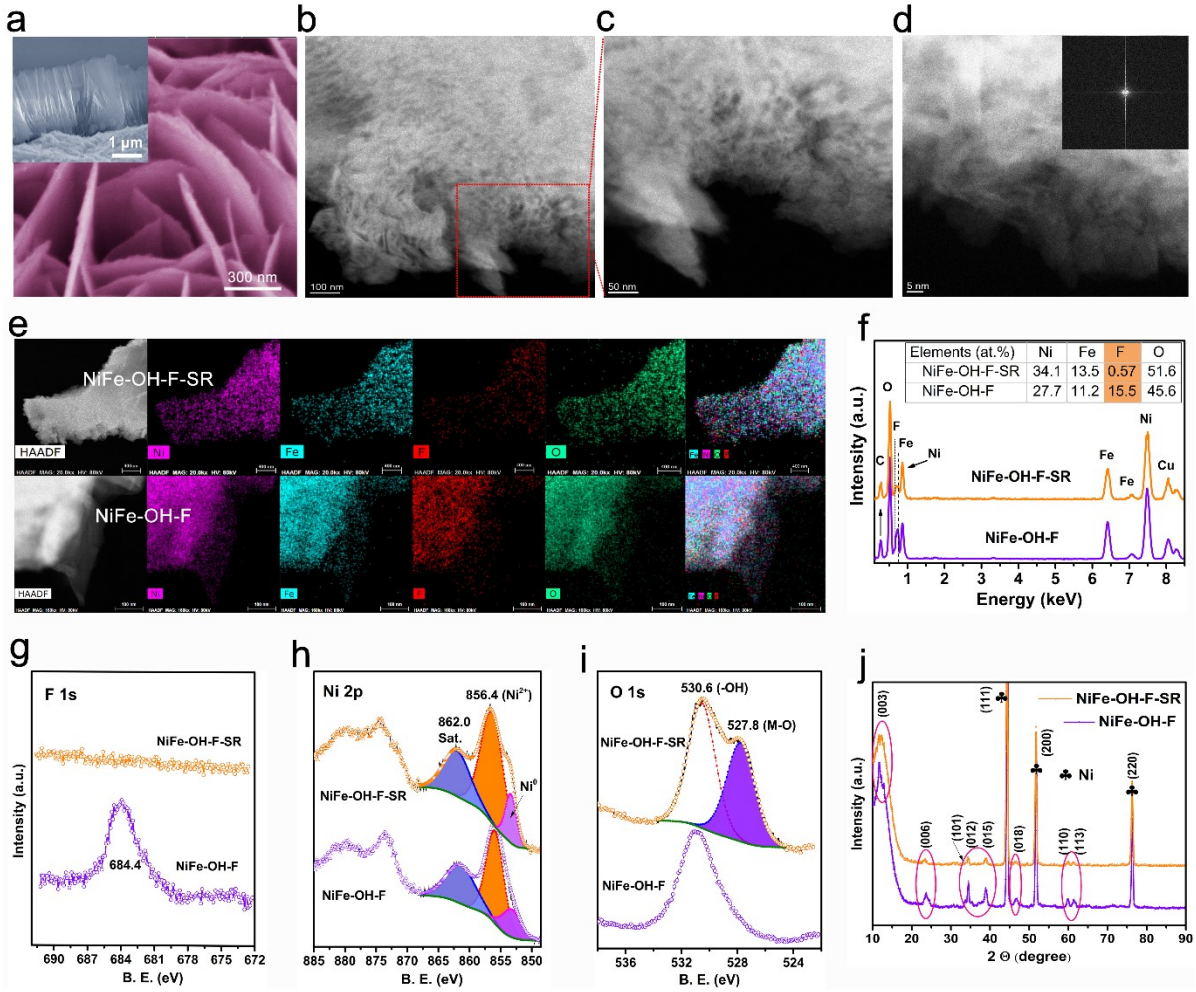

Figure 3. Characterizations of NiFe-OH-F-SR and NiFe-OH-F. (a) SEM images and (b-d) HAADF-STEM images of NiFe-OH-F-SR; Insets in (a) and (d) are the side-view of NiFe-OH-F-SR layer and the FFT image, respectively. (e) Elemental mapping images and (f) EDX spectra. The scale bars in the HAADF-STEM images of NiFe-OH-F-SR and NiFe-OH-F in (e) are 400 nm and 100 nm, respectively. (g-i) High resolution XPS spectra of F 1s, Ni 2p, and O 1s. (j) XRD patterns showing weaker peaks in NiFe-OH-F-SR compared to NiFe-OH-F.

To investigate the changes happened in the post-cycling NiFe-OH-F nanosheets, the material's morphology was firstly characterized by SEM and HAADF-STEM. As shown in Figure 3a-e and Figure S5, the post-cycling electrode maintains the overall nanosheets morphology of NiFe-OH-F but its surface becomes rough in nanoscale. The HAADF-STEM images in Figure 3b-d further revealed the highly porous and sponge-like morphology of the post-cycling NiFe-OH-F nanosheet. The high-resolution HAADF-STEM images in Figure 3d and the corresponding FFT image suggest that the crystalline NiFe hydroxide was transformed into amorphous after surface reconstruction that occurred in the electrochemical tuning process. This NiFe-OH-F derived material NiFe-OH-F-SR (we use "SR" to designate the surface reconstruction from here on) was further characterized.

Energy Dispersive X-ray (EDX) elemental mapping and spectrum were employed to examine the composition before and after surface reconstruction. After transforming from NiFe-OH-F to NiFe-OH-F-SR, the elements of Ni, Fe, and O remained homogeneously distributed, however significant amount of fluoride was removed (Figure 3e). Note that part of the red spots in the mapping images of fluoride might be originated from Fe because their energy positions are very close (F Kα: 0.677 KeV, Fe Lα: 0.705 eV). Based on the EDX spectrum analysis (Figure 3f), the fluoride content decreased from 15.5 a.t.% in NiFe-OH-F to 0.57 a.t.% in NiFe-OH-F-SR, and the Ni/Fe ratio in NiFe-OH-F ($27.7/11.2 \approx 2.47$) is consistent with that in NiFe-OH-F-SR ($34.1/13.5 \approx 2.52$). As the fluoride cannot be detected by ICP-MS, the compositional change was further confirmed by the sensitive X-ray photoelectron spectroscopy (XPS) spectra. On the basis of the XPS spectra, the atomic ratio of Ni/Fe/F in NiFe-OH-F is about 1.80/0.73/1 (the ratio was normalized by F^-), in agreement with the above EDX results. The F 1s peak vanished (Figure 3g) while some other peak appeared in O1s spectra (Figure 3i) of NiFe-OH-F-SR.[37] The disappearance of fluoride illustrates

that the *in situ* surface reconstruction during electrochemical tuning might be induced by fluoride leaching. The peaks of Ni $2p_{3/2}$ were located at 856.4 eV and 862.0 eV (satellite), attributed to Ni (II)-OH.[9,19,38] The small peak at about 853.4 eV appeared in Ni $2p_{3/2}$ can be assigned to metallic Ni^0 from Ni foam substrate.[17] Compared to the main peak of –OH (530.6 eV) in NiFe-OH-F, the emergence of the peak at 527.8 eV is corresponding to metal oxide ($NiFeO_x$) in NiFe-OH-F-SR.[23] The derived $NiFeO_x$ can be assigned to the chemical evolution that was aroused by fluoride leaching in NiFe-OH-F. The vanishing of fluoride was further confirmed by the XPS survey spectra in Figure S6a. XPS spectra of Fe 2p (Figure S6b) did not showed apparent change before and after the electrochemical tuning. Moreover, X-ray diffraction (XRD) was carried out to further reveal the evolution process. As shown in Figure 3j, the incorporation of fluoride does not affect the hydroxide nature of NiFe-OH-F: the peaks locate at 11.8°, 23.6°, 33.7°, 34.5°, 38.9°, 46.9°, 59.8°, 61.4° are well indexed to the facets of (003), (006), (101), (012), (015), (018), (110), (113) of NiFe hydroxide,[28,29] respectively. The (101) facet in XRD pattern is consistent with the observed lattice spacing in the high resolution HAADF-STEM image of NiFe-OH-F (Figure 1d). The three major peaks at 44.7°, 52°, and 76.5° are originated from the bottom Ni foam substrate. However, the NiFe-OH-F-SR shows much weaker crystalline features, consistent with the observed amorphous surface by STEM (Figure 3d). We also synthesized NiFe-OH-Cl and Co-OH-F on Ni foams by the similar hydrothermal method and cycled them in 1M KOH, but no significant improvements of the OER performance were observed (Figure S7). Based on the above analysis, we can safely conclude that the surface crystalline NiFe-OH-F has been converted into amorphous oxide. The HAADF-STEM image of the post-cycling NiFe-OH-F-SR shown in Figure S8 further confirms its core-shell structure, with the thickness of the surface amorphous layer measured as ~35 nm. It is difficult to completely convert the as-synthesized NiFe-OH-F into the amorphous

sponge-like structure due to the electrical/diffusional limitations. These limitations generally depend on the conductivity, porosity, thickness etc. of the electrocatalyst.[39] It is important to note that owing to its weak mechanical stability, a completely converted sponge-like nanostructure is less desirable than the as-obtained core-shell nanostructure. Moreover, the interface effect between original NiFe-OH-F core and the reconstructed layer can be excluded from the reasons that responsible for the high activity because the hetero-interface was formed in the 1st CV cycle and existed in the whole increase process of OER activity (Figure 2a and b). The NiFe-OH-F-SR nanosheets therefore demonstrate lower degree of crystallinity, different chemical composition, and more porous characteristics than NiFe-OH-F, indicating that the *in situ* dynamic surface self-reconstruction induced by fluoride leaching has great impacts on the crystallinity, chemical composition, and morphology of nanomaterials.

As the ratio of metal cation to fluoride may influence the catalytic performance and various ratios were reported for hydrothermally synthesized metal hydroxides nanostructures,[19,28,40–42] the influence of different NH_4F amounts on the OER performances of surface-reconstructed NiFe hydroxide needs to be studied. Note that no NH_4^+ or N element was included in the hydrothermal product of NiFe-OH-F. We initially reduced the amount of fluoride to 1/4 of that in the above NiFe-OH-F without altering the total amount of metal cations and then recorded the corresponding electrode's OER plots after 500 CV cycles (see details from the experimental methods). As shown in Figure S9, the OER activity and onset potential of the 1/4 × fluoride electrode is slightly lower than the NiFe-OH-F-SR electrode (1 × fluoride). We then increased the amount of NH_4F to 2 and 3 folds, respectively, and found that the OER activities of the 2 × fluoride and 3 × fluoride electrodes are much lower than NiFe-OH-F-SR even after 500 CV cycles (Figure S9). To further confirm the effects of fluoride in the electrochemical surface reconstruction, we synthesized NiFe

hydroxide (NiFe-OH) nanosheets on Ni foam without incorporating fluoride and conducted the electrochemical test under the same conditions. Figure S10a reveals that the morphology of NiFe-OH layer is similar with NiFe-OH-F. We performed the same CV cycling with NiFe-OH electrode but observed very different results than that on NiFe-OH-F. As shown in the Figure S10b, the oxidative peak gradually increased only in the first 8 cycles and then started decreasing from the 9th cycles until the peak was unnoticeable. This decrease is consistent with the reported phenomenon in Ni(Fe)OOH.[43] Moreover, the overall OER current density is relatively stable during the whole cycling process. Its OER current density at η = 220 mV (~ 7.4 mA cm^{-2}) is much lower than NiFe-OH-F-SR (76.8 mA cm^{-2}), despite the as-synthesized NiFe-OH shows a slightly better OER performance than that of the as-synthesized NiFe-OH-F. We then measured the electrochemical impedance spectroscopy (EIS) of NiFe-OH and NiFe-OH-F electrodes at the potential of 1.55 V vs RHE, respectively. The Nyquist plot of NiFe-OH shows a slightly smaller semicircle in the low-frequency region compared to NiFe-OH-F (Figure S10c), revealing that the NiFe-OH electrode has lower charge transfer resistance during the OER process. Compared to the NiFe-OH-F electrode, the slightly higher performance of the as-synthesized NiFe-OH might be originated from the higher charger transfer ability. Finally, the XRD measurements were conducted, the peak intensity difference between the as-synthesized NiFe-OH and post-cycling NiFe-OH are negligible (Figure S10d). The OER performance and good stability of NiFe-OH are consistent with previous reports.[7,31,33] The significant differences in the post-cycling NiFe-OH and post-cycling NiFe-OH-F (NiFe-OH-F-SR) demonstrates the crucial role of fluoride in surface self-reconstruction.

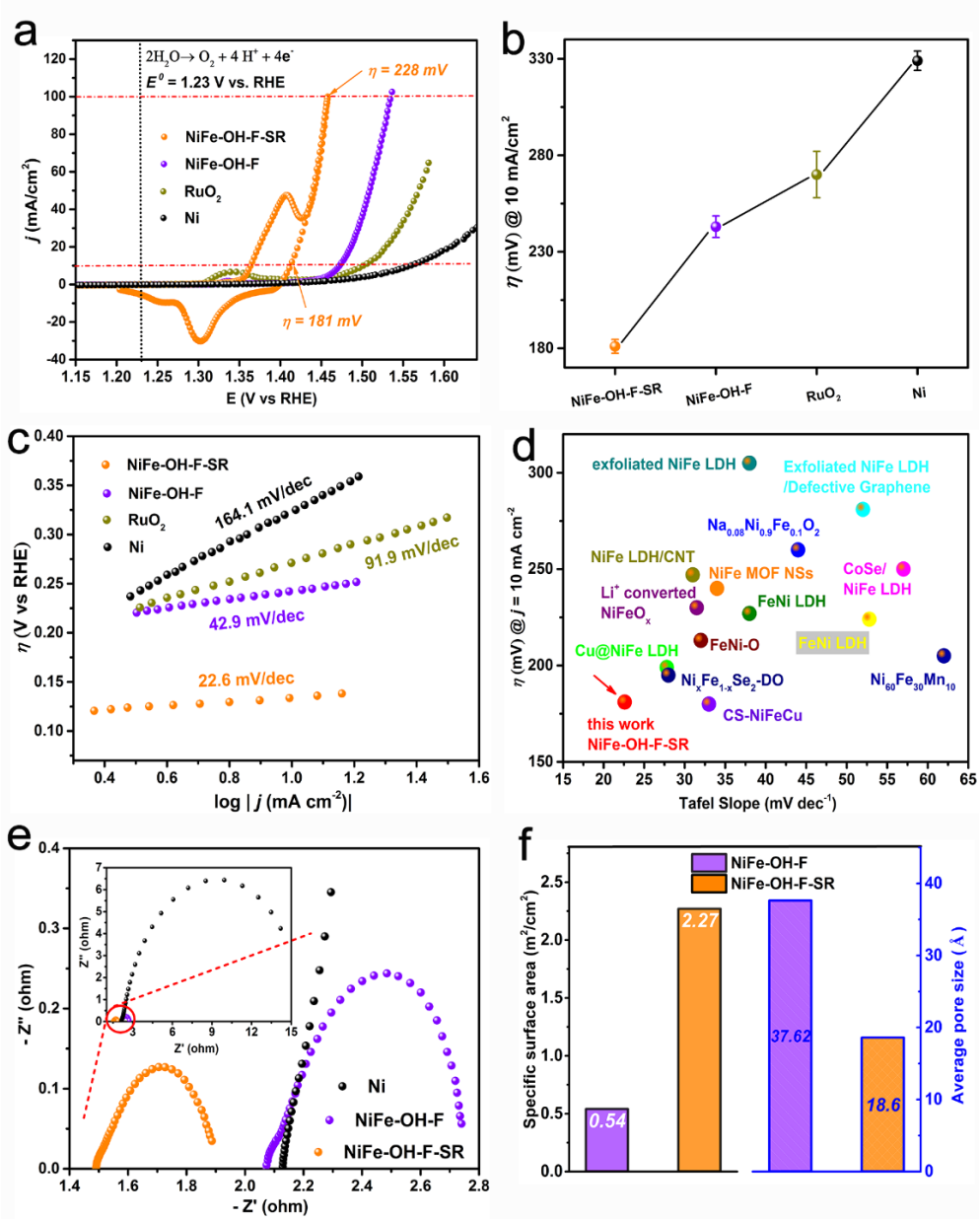

Figure 4. Electrochemical characterizations and Brunauer–Emmett–Teller tests. (a) CV/LSV plots; (b) η required for j = 10 mA cm^{-2}; and (c) Tafel slopes of NiFe-OH-F-SR, NiFe-OH-F, RuO_2, and Ni foam. (d) Comparison with state-of-the-art OER electrocatalysts. (e) EIS curves recorded at 1.55 V_{RHE}. (f) Specific surface area and average pore size of NiFe-OH-F-SR and NiFe-OH-F.

The electrocatalytic activities of NiFe-OH-F-SR, NiFe-OH-F, RuO_2, and Ni foam towards OER in 1M KOH were measured and compared. As shown in Figure 4a, NiFe-OH-F-SR is the best catalyst, giving much higher current density at the same overpotential. To reach the j = 10 mA cm^{-2}, NiFe-OH-F-SR required an extremely low overpotential of 181 mV (calculated from CV), which was 62, 89, and 148 mV less than that of NiFe-OH-F, RuO_2, and Ni foam, respectively (Figure 4b). At the j = 100 mA cm^{-2}, a low overpotential of 228 mV was needed by NiFe-OH-F-SR. A slightly lower overpotential of ~ 176 mV at 10 mA cm^{-2} was measured by a constant current method, as shown in the Figure S11. By plotting η against log (j), the kinetic parameter (Tafel slope) of OER by the four catalysts were calculated (Figure 4c). The NiFe-OH-F-SR has the lowest Tafel slope of 22.6 mV dec^{-1} compared to the other catalysts (42.9 ~ 164.1 mV dec^{-1}). In fact, as shown in Figure 4d (see details in Table S2), both the overpotential and Tafel slope of NiFe-OH-F-SR are superior to the reported state-of-the-art OER electrocatalysts.

To gain more insights into the OER reaction kinetics, EIS tests were performed as well. The Nyquist plot of NiFe-OH-F-SR shows a much smaller semicircle in the low-frequency region compared to NiFe-OH-F (Figure 4e), revealing that the dynamic surface self-reconstruction lowered the charge transfer resistance during the OER process. The intercept of the Nyquist plot with the real axis (- Z') in the high-frequency region represents the ohmic resistance (R_Ω), which is the sum of the electrode and solution resistances. We can observe that the R_Ω of NiFe-OH-F-SR electrode is smaller than that of NiFe-OH-F, revealing that the NiFe-OH-F-SR electrode has higher electrical conductivity than NiFe-OH-F.[13] To exclude the effect from Ni foam substrate, we also tested its EIS plots before and after the CV cycling at 1.5 and 1.6 V_{RHE}, respectively, and did not observed significant differences, as shown in Figure S12. This result suggests that the increased electrical conductivity in NiFe-OH-F-SR electrode is aroused by the reconstructed surface layer

rather than Ni foam substrate. The surface amorphous layer plays an important role in improving the conductivity of the NiFe-OH-F-SR as compared to the crystalline NiFe-OH-F. This is because the amorphous phase is defect-rich and the high defect concentration has been shown to greatly enhance the electrical conductivity of metal hydroxides.[43-45] In summary, we can conclude that the surface self-reconstruction enhances charge transfer during OER and the electrical conductivity of NiFe-OH-F-SR. The efficient OER activity of NiFe-OH-F-SR can be partially ascribed to these benefits.

We then compared the electrochemical surface area (ECSA) by estimating the double layer capacitance (C_{dl}) of the electrodes (see details from the supporting information) owing to the exposed surface sites to electrolyte can reflect the real surface area.[19,23,25] As shown in Figure S13, NiFe-OH-F shows a slightly lower ECSA (0.18 mF cm^{-2}) than bare Ni foam (0.25 mF cm^{-2}). The reason for this behavior is that the NiFe-OH-F layer has low conductivity in the potential range we measured, and then the good permeability of the NiFe-OH-F layer enables the direct polarization of ions in the electrolyte against the Ni foam substrate.[46] After the surface self-reconstruction, the measured ECSA of NiFe-OH-F-SR was improved to 0.85 mF cm^{-2} that can be ascribed to the enhanced conductivity. To further clarify the effects of surface area, we tested the Brunauer-Emmett-Teller (BET) surface area of NiFe-OH-F-SR and NiFe-OH-F. From NiFe-OH-F to NiFe-OH-F-SR, the BET surface area was improved from 207.7 m^2 g^{-1} to 873.1 m^2 g^{-1} and the average pore size decreased by over 50% (Figure S14a and Figure 4f). The mesoporous feature is further demonstrated by the pore-size distribution curves of the NiFe-OH-F-SR, as shown in the Figure S14b. However, the fact that ECSA/BET surface area of NiFe-OH-F-SR is 4 ~ 5 times that of the NiFe-OH-F cannot be solely accountable for the 58-fold higher catalytic activity of the former. As BET surface area/ECSA (C_{dl}) normalized activities are believed to provide meaningful measures

for the catalytic activities,[11,47-50] we then normalized the polarization curves of NiFe-OH-F-SR and NiFe-OH-F by their ECSA/BET surface areas even if the ECSA of NiFe-OH-F might be higher than the measured value. As shown in Figure S15, the normalized intrinsic activity of NiFe-OH-F-SR is at least an order of magnitude higher than that of NiFe-OH-F. The capacitance charge density normalized activity is another widely used method for comparing the intrinsic activity as well, we then normalized the OER polarization curves of NiFe-OH-F and NiFe-OH-F-SR by their capacitance charger densities which calculated from the reduction peaks (see detail from the Figure S16).[51,52] However, the Figure S15b shows that the normalized OER activity of NiFe-OH-F is much higher than that of NiFe-OH-F-SR. As shown in the Figure S17, the OER current densities increase slightly from the 150th to 500th CV cycle but the capacitance charger densities increase significantly. Therefore, we can conclude that no linear correlation exists between the capacitance charge density and OER activity. This result is understandable due to: (1) the reduction peak area of Ni-based material is not only sensitive to the surface area but also the electrical conductivity, composition, etc.[53-57] (2) Both the Ni and Fe are thought of as the active centers in $NiFeO_xH_y$,[35,57-59] its active surface area could not be solely reflected by the capacitance charger density of Ni^{3+}/Ni^{2+} peak. Despite we cannot compare the intrinsic activity by the capacitance charger density normalization in $NiFeO_xH_y$, our analysis provides a reference for the selection of normalization method.

Excepting the BET surface area/ECSA (C_{dl}) normalized activities, the onset potential is another important parameter in judging the intrinsic activities of catalysts because it is not easy to be affected only by adjusting the surface area.[60-64] Thus, the improvement of intrinsic activity of NiFe-OH-F-SR can be reflected in the significantly reduced onset potential (> 50 mV, Figure 4a) compared to NiFe-OH-F, even if we calculate the onset potential by different ways.[65,66] As the

transformations in phase, composition, and structural size can significantly alter the intrinsic activity of catalysts,[11,60] the improvement of intrinsic activity in the dynamic surface reconstruction process can be understood. According to above analysis, the superior electrocatalytic activity of NiFe-OH-F-SR can be ascribed to the increased surface area, desirable nanostructure, the improved charger transfer ability, and the enhanced intrinsic activity.

For an electrocatalyst, the structural porosity, active sites, and electric conductivity are the critical factors for its catalytic performances. In the case of NiFe-OH-F-SR, there is no doubt that the intrinsic merits of all these factors greatly contribute to its excellent activity. The NiFe-OH-F-SR electrode is comprised of three levels of porous structures including the supporting supermacroporous nickel foam substrate (~ 300 μm), the vertically grown nanosheet arrays (300 ~ 500 nm), and the topmost *in situ* converted mesoporous network. After the *in situ* surface reconstruction, a high specific surface area of 873.1 $m^2 g^{-1}$ was achieved on NiFe-OH-F-SR. One of the major challenges of porous catalysts for electrocatalysis is that the very small pore size impedes the effective mass transport to the active sites and the diffusion of products, leading to limited electrode activity. The accumulation of product gas can block the active sites and then result in the structural collapse of the catalysts. Herein, the NiFe-OH-F-SR electrode has three levels of porosity and this hierarchical framework is beneficial for exposing catalytic active sites, enhancing mass transport, and accelerating dissipation of product bubbles and therefore assuring the high activity and durability. Besides, the conductivity and charge transfer ability are enhanced by the *in situ* surface reconstruction, as evidenced by the high kinetics and Nyquist plots.

In summary, using NiFe-OH-F as a representative example of transition metal hydroxide, we show that the fluoride leaching can trigger *in situ* dynamic surface self-reconstruction and convert the original NiFe-OH-F into highly porous and amorphous metal oxide under OER conditions. A

current density of 10 mA cm^{-2} is obtained at an overpotential of 176 mV in 1M KOH using the surface reconstructed NiFe-OH-F (NiFe-OH-F-SR) as the catalyst, making it one of the most active OER catalysts reported to date. This simple and scalable approach described here might be applicable for the synthesis of other amorphous metal oxide-based nanomaterials and provide a strategy to create highly active OER catalyst to enable the development of efficient water splitting systems, fuel cells, rechargeable metal-air batteries, and other energy conversion and storage devices.

ASSOCIATED CONTENT

Supporting Information.

Supporting Information Available: Additional details on the experimental materials and methods, Photographs, SEM, HAADF-STEM images showing the looks and morphologies of the samples. Electrochemical analysis and measurements are included. Table of ICP-MS tests showing the concentrations of Ni and Fe elements in the electrolyte after OER test. Comparison Table is also provided for better comparing the performance with the previously reported works.

AUTHOR INFORMATION

Corresponding Author

*E-mail: shanhu@iastate.edu

Funding Sources

This material is based upon the work supported by the U.S. National Science Foundation (Grant No. CMMI-1663509). B. Z. was supported by the Catron Fellowship from the College of Engineering, Iowa State University, United States.

Notes

The authors declare no competing financial interest.

ACKNOWLEDGMENT

The characterizations of HAADF-STEM and EDX were carried out in Ames National Lab, U.S. Department of Energy (DOE). SEM, EDX, XRD, and XPS characterizations were conducted in The Materials Analysis and Research Laboratory (MARL) of Iowa State University. We thank Prof. Hailiang Wang at Yale University for the helpful discussions and experimental help during the revision process. The ICP-MS tests were performed in Prof. Wenyu Huang's Lab at Iowa State University.

REFERENCES

(1) Zhao, S.; Wang, Y.; Dong, J.; He, C. T.; Yin, H.; An, P.; Zhao, K.; Zhang, X.; Gao, C.; Zhang, L.; et al. *Nat. Energy* **2016**, *1*, 1–10.

(2) Cook, T. R.; Dogutan, D. K.; Reece, S. Y.; Surendranath, Y.; Teets, T. S.; Nocera, D. G. *Chem. Rev.* **2010**, *110*, 6474–6502.

(3) Stamenkovic, V. R.; Strmcnik, D.; Lopes, P. P.; Markovic, N. M. *Nat. Mater.* **2016**, *16*, 57–69.

(4) Aurbach, D.; McCloskey, B. D.; Nazar, L. F.; Bruce, P. G. *Nat. Energy* **2016**, *1*, 1–11.

(5) Suen, N.-T.; Hung, S.-F.; Quan, Q.; Zhang, N.; Xu, Y.-J.; Chen, H. M. *Chem. Soc. Rev.* **2017**, *46*, 337–365.

(6) Tahir, M.; Pan, L.; Idrees, F.; Zhang, X.; Wang, L.; Zou, J. J.; Wang, Z. L. *Nano Energy* **2017**, *37*, 136–157.

(7) Lu, Z.; Xu, W.; Zhu, W.; Yang, Q.; Lei, X.; Liu, J.; Li, Y.; Sun, X.; Duan, X. *Chem. Commun.* **2014**, *50*, 6479–6482.

(8) Li, Z.; Shao, M.; An, H.; Wang, Z.; Xu, S.; Wei, M.; Evans, D. G.; Duan, X. *Chem. Sci.* **2015**, *6*, 6624–6631.

(9) Lu, X.; Zhao, C. *Nat. Commun.* **2015**, *6*, 6616.

(10) Dionigi, F.; Strasser, P. *Adv. Energy Mater.* **2016**, *6*, 1600621.

(11) Song, F.; Hu, X. *Nat. Commun.* **2014**, *5*, 1–9.

(12) Jia, Y.; Zhang, L.; Gao, G.; Chen, H.; Wang, B.; Zhou, J.; Soo, M. T.; Hong, M.; Yan, X.; Qian, G.; et al. *Adv. Mater.* **2017**, *29*, 1–8.

(13) Luo, Y.; Zhou, H.; Sun, J.; Qin, F.; Yu, F.; Bao, J.; Yu, Y.; Chen, S.; Ren, Z. *Energy Environ. Sci.* **2017**, *10*, 1820–1827.

(14) Wang, Y.; Qiao, M.; Li, Y.; Wang, S. *Small* **2018**, *1800136*.

(15) Xuan, C.; Wang, J.; Xia, W.; Zhu, J.; Peng, Z.; Xia, K.; Xiao, W.; Xin, H. L.; Wang, D. *J. Mater. Chem. A* **2018**, *00*, 1–8.

(16) Yue, Q.; Liu, C.; Wan, Y.; Wu, X.; Zhang, X.; Du, P. *J. Catal.* **2018**, *358*, 1–7.

(17) Hu, F.; Zhu, S.; Chen, S.; Li, Y.; Ma, L.; Wu, T.; Zhang, Y.; Wang, C.; Liu, C.; Yang, X.; et al. *Adv. Mater.* **2017**, *29*, 1–9.

(18) Yang, N.; Tang, C.; Wang, K.; Du, G.; Asiri, A. M.; Sun, X. *Nano Res.* **2016**, *9*, 3346–3354.

(19) Xu, X.; Song, F.; Hu, X. *Nat. Commun.* **2016**, *7*, 1–7.

(20) Zhang, B.; Xiao, C.; Xie, S.; Liang, J.; Chen, X.; Tang, Y. *Chem. Mater.* **2016**, *28*, 6934–6941.

(21) Zhang, B.; Lui, Y. H.; Ni, H.; Hu, S. *Nano Energy* **2017**, *38*, 553–560.

(22) Wang, Z.; Li, J.; Tian, X.; Wang, X.; Yu, Y.; Owusu, K. A.; He, L.; Mai, L. *ACS Appl. Mater. Interfaces* **2016**, *8*, 19386–19392.

(23) Xia, C.; Jiang, Q.; Zhao, C.; Hedhili, M. N.; Alshareef, H. N. *Adv. Mater.* **2016**, *28*, 77–85.

(24) Shi, Y.; Zhang, B. *Chem. Soc. Rev.* **2016**, *45*, 1529–1541.

(25) Chen, W.; Wang, H.; Li, Y.; Liu, Y.; Sun, J.; Lee, S.; Lee, J. S.; Cui, Y. *ACS Cent. Sci.* **2015**, *1*, 244–251.

(26) Wu, H.; Xu, M.; Wu, H.; Xu, J.; Wang, Y.; Peng, Z.; Zheng, G. *J. Mater. Chem.* **2012**, *22*, 19821.

(27) Jiang, J.; Liu, J. P.; Huang, X. T.; Li, Y. Y.; Ding, R. M.; Ji, X. X.; Hu, Y. Y.; Chi, Q. B.; Zhu, Z. H. *Cryst. Growth Des.* **2010**, *10*, 70–75.

(28) Liu, X.; Wang, X.; Yuan, X.; Dong, W.; Huang, F. *J. Mater. Chem. A* **2016**, *4*, 167–172.

(29) Zhang, B.; Lui, Y. H.; Zhou, L.; Tang, X.; Hu, S. *J. Mater. Chem. A* **2017**, *5*, 13329–13335.

(30) Zhang, B.; Hu, S. *Electrochem. commun.* **2018**, *86*, 108–112.

(31) Yan, K.; Lafleur, T.; Chai, J.; Jarvis, C. *Electrochem. commun.* **2016**, *62*, 24–28.

(32) M. Gong, Y. Li, H. Wang, Y. Liang, J. Z. Wu, J. Zhou, J. Wang, T. Regier, F. Wei, H. D. *J. Am. Chem. Soc.* **2013**, *135*, 8452–8455.

(33) Chen, S.; Duan, J.; Bian, P.; Tang, Y.; Zheng, R.; Qiao, S. Z. *Adv. Energy Mater.* **2015**, *5*, 1–7.

(34) Friebel, D.; Louie, M. W.; Bajdich, M.; Sanwald, K. E.; Cai, Y.; Wise, A. M.; Cheng, M. J.; Sokaras, D.; Weng, T. C.; Alonso-Mori, R.; et al. *J. Am. Chem. Soc.* **2015**, *137*, 1305–1313.

(35) Görlin, M.; Chernev, P.; De Araújo, J. F.; Reier, T.; Dresp, S.; Paul, B.; Krähnert, R.; Dau, H.; Strasser, P. *J. Am. Chem. Soc.* **2016**, *138*, 5603–5614.

(36) Louie, M. W.; Bell, A. T. *J. Am. Chem. Soc.* **2013**, *135*, 12329–12337.

(37) Chen, L. F.; Yu, Z. Y.; Wang, J. J.; Li, Q. X.; Tan, Z. Q.; Zhu, Y. W.; Yu, S. H. *Nano Energy* **2015**, *11*, 119–128.

(38) Wang, H.; Lee, H. W.; Deng, Y.; Lu, Z.; Hsu, P. C.; Liu, Y.; Lin, D.; Cui, Y. *Nat. Commun.* **2015**, *6*.

(39) Godwin, I.; Rovetta, A.; Lyons, M.; Coleman, J. *Curr. Opin. Electrochem.* **2018**, *7*, 31–35.

(40) Yang, Y.; Dang, L.; Shearer, M. J.; Sheng, H.; Li, W.; Chen, J.; Xiao, P.; Zhang, Y.; Hamers, R. J.; Jin, S. *Adv. Energy Mater.* **2018**, *1703189*.

(41) Zhao, J.; Li, C.; Zhang, Q.; Zhang, J.; Wang, X.; Sun, J.; Wang, J.; Xie, J.; Lin, Z.; Li, Z.; et al. *Nano Res.* **2017**, 1–12.

(42) Yao, S. *Int. J. Electrochem. Sci.* **2018**, *13*, 542–550.

(43) Li, H.; Gao, Y.; Wang, C.; Yang, G. *Adv. Energy Mater.* **2015**, *5*, 1–9.

(44) Li, H. B.; Yu, M. H.; Wang, F. X.; Liu, P.; Liang, Y.; Xiao, J.; Wang, C. X.; Tong, Y. X.; Yang, G. W. *Nat. Commun.* **2013**, *4*, 1–7.

(45) Bernard, M. C.; Cortes, R.; Keddam, M.; Takenouti, H.; Bernard, P.; Senyarich, S. *J. Power Sources.* **1996***, 63,* 247-254.

(46) Batchellor, A. S.; Boettcher, S. W. *ACS Catal.* **2015**, *5*, 6680–6689.

(47) Zhang, B.; Zheng, X.; Voznyy, O.; Comin, R.; Bajdich, M.; Arquer, F. P. G. De; Dinh, C. T.; Fan, F.; Yuan, M.; Janmohamed, A.; et al. *Science* **2016**, *352*, 333–338.

(48) Xu, L.; Jiang, Q.; Xiao, Z.; Li, X.; Huo, J.; Wang, S.; Dai, L. *Angew. Chemie Int. Ed.* **2016**, *55*, 5277–5281.

(49) Suntivich, J.; May, K. J.; Gasteiger, H. a; Goodenough, J. B.; Shao-horn, Y. *Science* **2011**, *334*, 2010–2012.

(50) L. C. Seitz, C. F. Dickens, K. Nishio, Y. Hikita, J. Montoya, A. Doyle, C. Kirk, A. Vojvodic, H. Y. Hwang, J. K. Norskov, T. F. J. *Science* **2016**, *353*, 1011–1014.

(51) Huang, W.; Ma, X. Y.; Wang, H.; Feng, R.; Zhou, J.; Duchesne, P. N.; Zhang, P.; Chen, F.; Han, N.; Zhao, F.; et al. *Adv. Mater.* **2017**, *29*, 1–8.

(52) Xu, D.; Stevens, M. B.; Rui, Y.; DeLuca, G.; Boettcher, S. W.; Reichmanis, E.; Li, Y.; Zhang, Q.; Wang, H. *Electrochim. Acta* **2018**, *265*, 10–18.

(53) Shalom, M.; Ressnig, D.; Yang, X.; Clavel, G.; Fellinger, T. P.; Antonietti, M. *J. Mater. Chem. A* **2015**, *3*, 8171–8177.

(54) Wang, Y.; Gai, S.; Niu, N.; He, F.; Yang, P. *J. Mater. Chem. A* **2013**, *1*, 9083–9091.

(55) Salunkhe, R. R.; Lin, J.; Malgras, V.; Dou, S. X.; Kim, J. H.; Yamauchi, Y. *Nano Energy* **2015**, *11*, 211–218.

(56) Trotochaud, L.; Young, S. L.; Ranney, J. K.; Boettcher, S. W. *J. Am. Chem. Soc.* **2014**, *136*, 6744–6753.

(57) Stevens, M. B.; Trang, C. D. M.; Enman, L. J.; Deng, J.; Boettcher, S. W. *J. Am. Chem. Soc.* **2017**, *139*, 11361–11364.

(58) Chen, J. Y. C.; Dang, L.; Liang, H.; Bi, W.; Gerken, J. B.; Jin, S.; Alp, E. E.; Stahl, S. S. *J. Am. Chem. Soc.* **2015**, *137*, 15090–15093.

(59) Hunter, B. M.; Winkler, J. R.; Gray, H. B. *Molecules* **2018**, *23*, 93.

(60) Li, C.; Han, X.; Cheng, F.; Hu, Y.; Chen, C.; Chen, J. *Nat. Commun.* **2015**, *6*, 1–8.

(61) Chung, H. T.; Won, J. H.; Zelenay, P. *Nat. Commun.* **2013**, *4*, 1922–1925.

(62) Wu, Z. Y.; Xu, X. X.; Hu, B. C.; Liang, H. W.; Lin, Y.; Chen, L. F.; Yu, S. H. *Angew. Chemie - Int. Ed.* **2015**, *54*, 8179–8183A.

(63) Jin, Y.; Wang, H.; Li, J.; Yue, X.; Han, Y.; Shen, P. K.; Cui, Y. *Adv. Mater.* **2016**, *28* (19), 3785–3790.

(64) Liu, Y.; Liang, X.; Gu, L.; Zhang, Y.; Li, G.-D.; Zou, X.; Chen, J.-S. *Nat. Commun.* **2018**, *9*, 2609.

(65) Botz, A. J. R.; Nebel, M.; Rincón, R. A.; Ventosa, E.; Schuhmann, W. *Electrochim. Acta* **2015**, *179*, 38–44.

(66) Chen, Z.; Jaramillo, T.F.; Deutsch, T.G.; Kleiman-Shwarsctein, A.; Forman, A.J.; Gaillard, N.; Garland, R.; Takanabe, K.; Heske, C.; Sunkara, M.; McFarland, E.W. *J. Mater. Res.* **2010**, *25*, 3-16.

SYNOPSIS

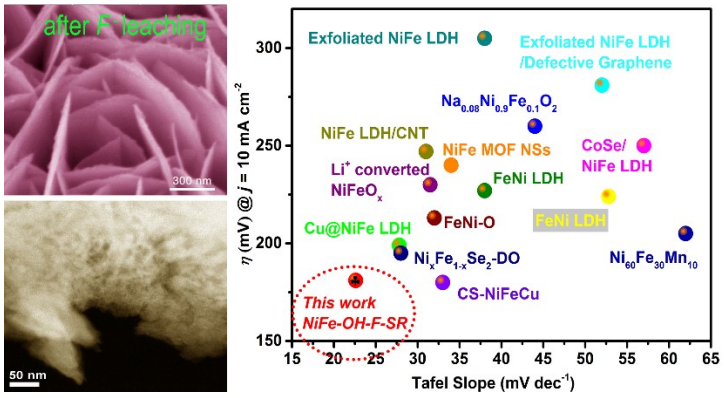
after F⁻ leaching
300 nm
50 nm
Exfoliated NiFe LDH
Exfoliated NiFe LDH /Defective Graphene
Na0.08Ni0.9Fe0.1O2
NiFe LDH/CNT
NiFe MOF NSs
CoSe/ NiFe LDH
Li+ converted NiFeOx
FeNi LDH
FeNi-O
FeNi LDH
Cu@NiFe LDH
NixFe1-xSe2-DO
Ni60Fe30Mn10
CS-NiFeCu
This work NiFe-OH-F-SR
η (mV) @ j = 10 mA cm-2
Tafel Slope (mV dec-1)
300
250
200
150
15
20
25
30
35
40
45
50
55
60
65